PAPER • OPEN ACCESS

Visually clear diffusive light panel with embedded semi-reflective rough-surface planar outcouplers

View the article online for updates and enhancements.

Visually clear diffusive light panel with embedded semi-reflective rough-surface planar outcouplers

Hongbae Park[1,*] and **Boris Stoeber**[1,2]

[1] Department of Electrical and Computer Engineering, The University of British Columbia, Vancouver, BC, Canada
[2] Department of Mechanical Engineering, The University of British Columbia, Vancouver, BC, Canada

E-mail: hongbae@ece.ubc.ca

Abstract

We present a visually transparent light-diffusing panel in the form of a light guide, which has semi-reflective, thin-film blades buried within it acting as diffusive outcouplers. The semi-reflective blades can be tilted relative to the length of the light guide and are textured to partially scatter the light incident upon them in the reflection domain, while transmitting the rest. We show that the texturization of the outcouplers can be achieved following a simple molding process using a mold with well-defined roughness regions to subsequently create light-scattering surfaces. The mold is either based on frosted glass or on a photolithographic process using a polymer photomask. We demonstrate with a prototype that the view through the textured outcouplers is visually clear. Also, we demonstrate that by varying the angular difference between the incidence of the propagating light rays and the outcoupler angle, the ratio of the amount of diffused light emanating from the two surfaces of the light guide can be biased from ∼1:2 to ∼1:20. The proposed device can be used as a transparent light source that provides an occlusion-free and undistorted see-through view.

Keywords: diffuser, light guide, photolithography, transparent

(Some figures may appear in colour only in the online journal)

1. Introduction

Thin, visually transparent lighting panels that can redirect, reshape, and/or diffuse light in an engineered fashion when illuminated have been attracting attention lately. Such panels can find useful applications in many areas ranging from augmented reality devices [1–6], transparent displays [7–9], solar energy harvesting [10, 11], and indoor lighting [7, 12, 13]. Numerous novel ideas have been put forth in the making of such light-emitting transparent panels, which can be categorized into a few major groups based on their working principles. The most straightforward implementations are based on surface relief or embedded physical perturbations, on or within a transparent substrate, using micro-features [1, 2, 7, 10, 13–18], particles [8, 12], and/or buried reflecting surfaces [3, 4] that abruptly disturb the propagation of light that interacts with them. These approaches can be well-suited in applications that work with a broad spectrum of light. However, the fabrication processes of these devices can be oftentimes complex, inhibiting high-volume production unless replication through nano-imprinting or similar processes can be considered. Also, the embedded micro-features or particles disturb light transmission through the panel, which may be of
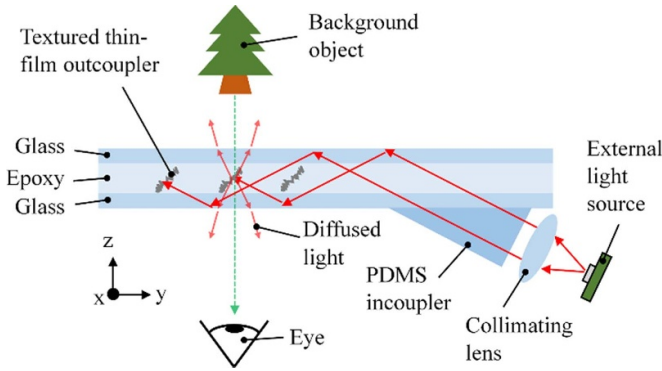
Figure 1. A side-view schematic of a light guide with embedded tilted diffusive outcouplers.

Figure 2. Micrograph of a PET photomask including air bubbles appearing as speckles. The white scale bar is 200 μm in length. The text is on the bottom side.

Figure 3. Simplified cross-sectional view of a photoresist film exposed through a PET photomask with air bubbles buried in it.

concern if transparency of the device is required. Another group of devices uses diffractive [5, 11] or holographic [6] structures that can precisely control the light output while offering good light transmission. However, holographic and diffractive structures typically also require specific illumination conditions regarding the wavelength and the incident angle of the light. Another method was recently demonstrated, using resonant nanoparticles [9] infused in a transparent substrate. However, the resonance-based scattering is wavelength dependent, therefore the broadband outcoupling efficiency is limited.

In this paper, we introduce a novel texturization process for creating a diffusive surface for diffusively decoupling light from a light guide allowing for a variable output ratio top-to-bottom, while preserving the see-through transparency of the light guide; both these features are demonstrated through prototypes. A simplified schematic of the prototype in figure 1 shows textured semi-reflective thin-film outcouplers that are embedded in a visually transparent epoxy layer, providing an undistorted view through the panel. Light from a light-emitting diode (LED) source is coupled into the light guide via a prism incoupler and travels through the light guide by total internal reflection (TIR). The light bound within the light guide eventually reaches the textured surface which breaks out the light to produce diffuse illumination. The fabrication of the textured, diffusive outcouplers utilizes a molding process and sputter deposition. One advantage of this approach we wish to highlight lies in its simplicity, which can facilitate a seamless integration into other fabrication processes, where formation of a textured surface is needed. As well, such transparent and diffusive surface can be used as a passive lighting panel that can double as a window or a skylight, or as a light source in a transparent near-eye display concept that was introduced previously [19].

2. Surface texturization methods and prototype

The texturized surface is generated though a molding process. The mold is prepared through one of two methods: (1) a photolithography process leads to planar molds with well-defined
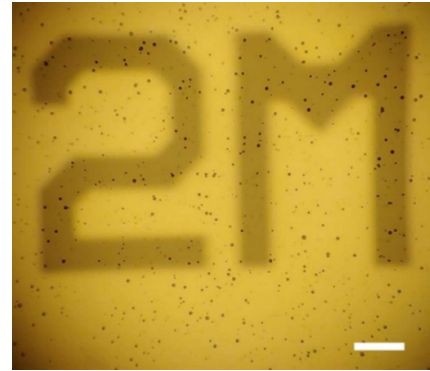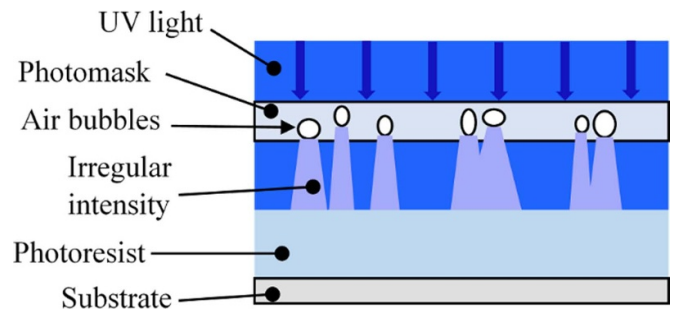
outlines, or (2) the rough surfaces of commercial frosted glass plates can be arranged at well-defined angles, albeit without the flexibility of defining an arbitrary outline of the structures.

2.1. Photolithographic surface texturization and characterization of the surface roughness

The underlying principle of the photolithography-based fabrication method is very straightforward. The polyethylene terephthalate (PET) photomask (Fujifilm HPR-7S) has tiny air bubbles trapped in it that are tens of microns in size or smaller as shown in figure 2. When a layer of negative photoresist is exposed through the PET photomask, the air bubbles scatter the light transmitted through, creating an irregular intensity profile across the photoresist leading to a textured surface of the partially underexposed photoresist as shown in figure 3.

We characterize the effect of exposure time and the number of photomask layers on photoresist roughness. We start by spin-coating a layer of OmniCoat (Kayaku Advanced Materials Inc., Kayaku from hereon) on a clean 100 mm fused silica wafer, to promote adhesion between the wafer and photoresist. The wafer is then baked at 200 °C for 1 min. Next, SU-8 (Kayaku) is spin-coated at 3700 rpm, and pre-baked at 65 °C for 1 min then at 90 °C for 3 min. This creates a ∼6 μm SU-8 film which we expose using a Neutronix-Quintel NxQ4006 mask aligner and an h-line source with an average intensity of ∼20 mW cm^{-2}. To evaluate the effect of exposure time and
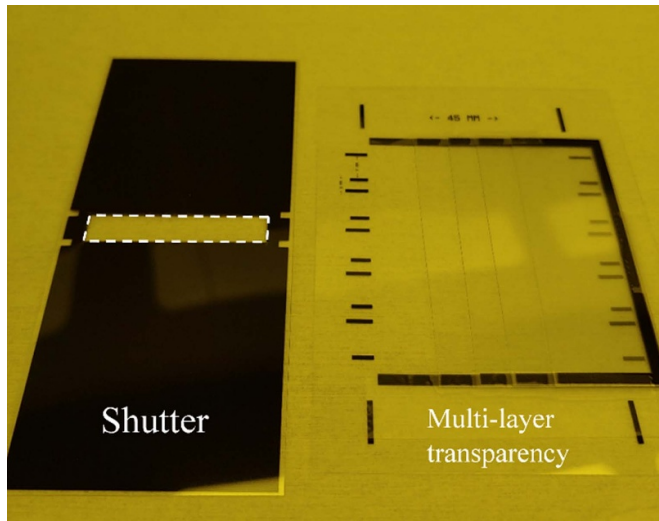
Figure 4. A transparency shutter system used to create tiles of distinctively exposed areas. The rectangular area of the shutter highlighted in a dashed line on the left has been cut out to form a window. The shutter is placed over the multi-layer transparency on the right and is scrolled up or down to expose different areas of a wafer at different exposure times.
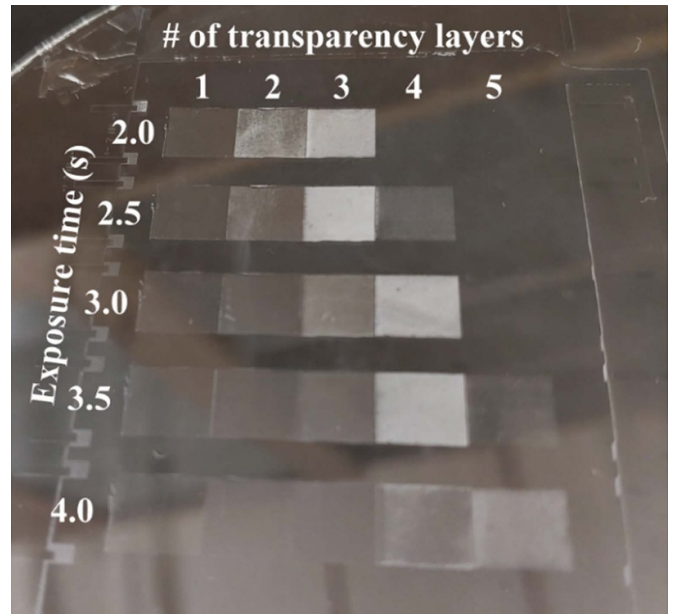

Figure 5. A fused-silica wafer coated with a 6 μm SU-8 film exposed with different combinations of exposure time and number of photomask layers. Each square 'tile' with a different level of fuzziness is about 7 mm × 7 mm in size.

the photomask layer count, we expose different sections of the SU-8 film in different combinations of the exposure time and the number of photomask layers, using a shutter system shown in figure 4. The multi-layer transparency consists of a stack of an increasing number of photomask layers from left (1) to right (5), while the shutter is used to expose a rectangular region of the photoresist across the different layer thicknesses at a time at exposure times between 2 and 4 s. This forms a grid of 'tiles' each ultimately having a different level of roughness, hence light diffusivity. After exposure, the wafer is post-baked using the same baking schedule as the pre-bake. The wafer is developed for 20 s using an SU-8 developer (Kayaku). Figure 5 shows the wafer after development, and figure 6 shows how some of the tiles are optically clear while others are diffusive against a background with text.

The surface roughness of the textured areas is measured by probing in 1D the surface topology of each tile using a Dektak XT stylus profilometer. Figure 7 shows the measured average surface roughness Ra of the tiles represented as a colormap. Note that the surface roughness does not correlate to the degree of diffusiveness of the surface. For example, the tile exposed for 2.5 s using 5 photomask layers appear to be transparent (see figures 4 and 5), but its surface roughness is comparable to the tile exposed for 3.0 s using 2 photomask layers that appears translucent. This is because in the case of the latter, the surface topology of the textured area consists of rolling ups and downs with a relatively small variation in height, whereas in the former the textured area consists of flat patches where underexposed SU-8 is washed away, at the same time having sharp, tall features that increase the average roughness. The visual appearance of the textured surface on the other hand can be a good first-pass indication of how diffusive the surface is, e.g. how clear an object behind the surface appears (as in figure 6) where more light is being scattered if the object
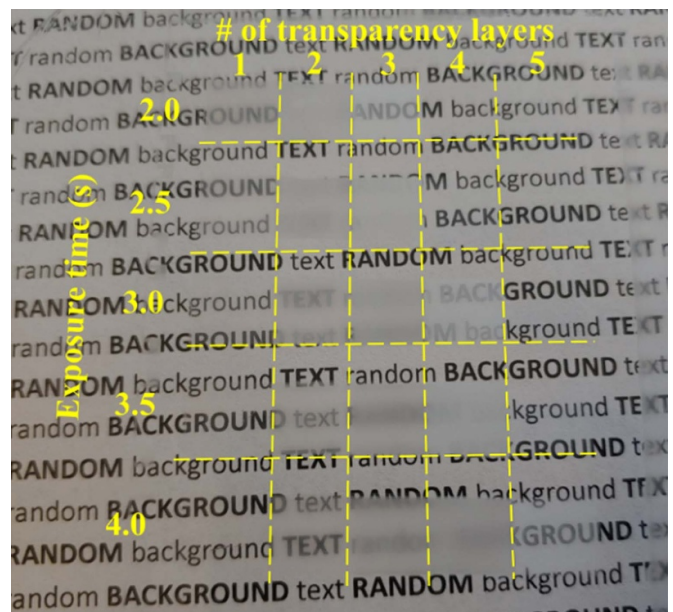
Figure 6. The wafer in figure 5 held over a background with text to show how diffusive each tile is. Dashed lines are added to mark the boundaries between the tiles.

appears less clear. As such, a textured surface such as the one exposed with 2 transparency layers for 2.0 s (see figure 6) is suitable for our applications.

We make a prototype device to showcase the transparent diffuser concept with the diffusive surface fabricated using the photolithography-based surface texturing. First, we texturize a 20 mm × 20 mm area on a 4 inch silicon wafer using the above-mentioned process involving an SU-8 film with 2

Figure 7. Average surface roughness Ra of each translucent tile on the wafer shown in figure 5.
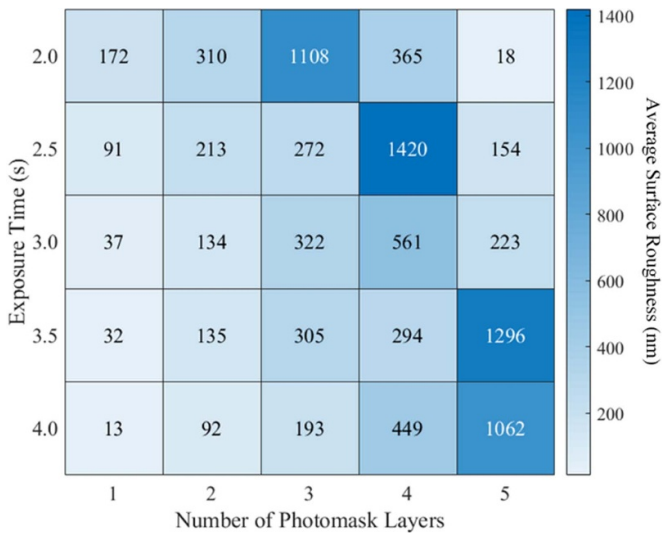
transparency layers exposed for 2 s. Then, to replicate the texture, an epoxy resin (MAX CLR from Polymer Inc.) is poured over the textured area, and a 2" × 3" glass slide is put on top to spread out the resin. After the resin is cured for 48 h, the resin and the glass slide are pried from the silicon wafer, and excess cured resin around the edges of the glass slide is trimmed off. Then, an 8 nm aluminum film is sputter coated on the cured resin using an Angstrom Engineering Aeres physical-vapor deposition (PVD) sputter coater, to make the textured area semi-reflective. Immediately after sputtering, the same epoxy resin is poured on the aluminum film to encapsulate it, and another glass slide is placed on top to make a sandwich of glass slides for a total thickness of ∼2 mm. The finished prototype is shown in figure 8.

2.2. Texturization on angled surfaces using frosted glass slides and casting

The lithography-based surface texturization method offers a great flexibility in choosing various combinations of surface roughness and optical clarity. However, it is not trivial to texturize tilted surfaces using the same method especially if multiple tilted surfaces are arranged in a discontinuous array, such as the proposed outcouplers shown in figure 1.

To texturize an array of tilted surfaces, we first make a staircase-like stack of 25 mm × 75 mm × 1 mm glass slides with frosted ends (Globe Scientific 1324W) as shown in figure 10(A). The frosted section of the glass slides has an average RMS surface roughness of around 300 nm, measured by probing with a Dektak XT mechanical profilometer. Polydimethylsiloxane (PDMS) is applied between the glass slides to bond them together (figures 9(A) and (B)). The glass slides are offset from each other by 2.08 mm on the short edge such that the side of the stack forms a stair inclined at a ∼30° angle, taking into account the thickness of PDMS (∼0.2 mm) between
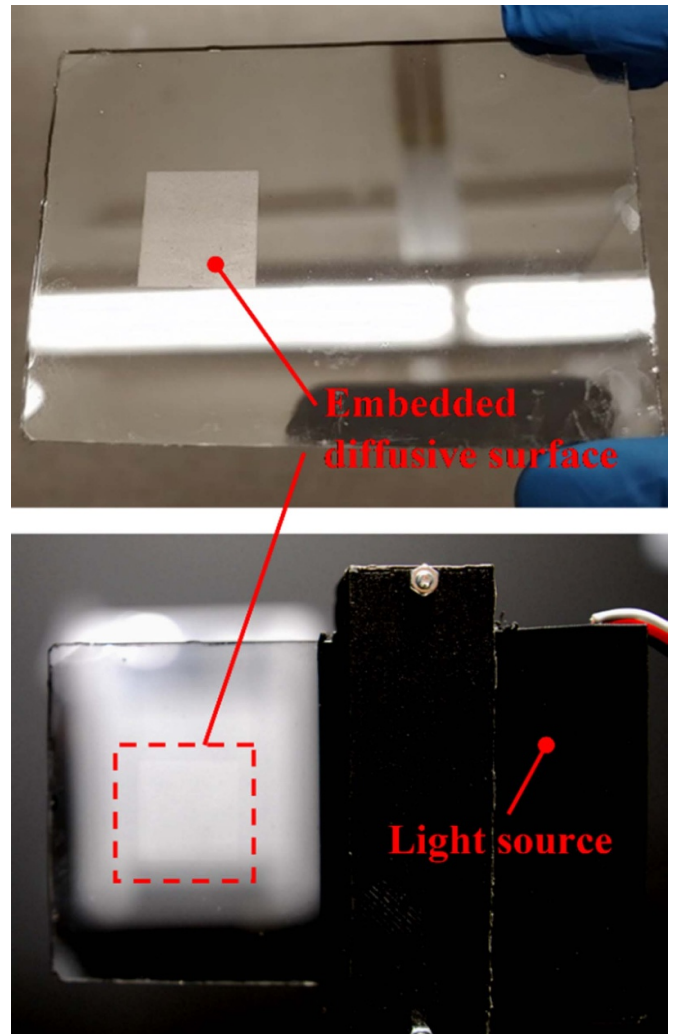

Figure 8. Finished light guide prototype with an embedded planar semi-reflective aluminum film, fabricated using a photolithography-based process. Top: the prototype itself. Bottom: the prototype is hooked up to a light source for coupling light into the prototype.

the glass slides. All glass slides are oriented identically with the frosted section on the same end of the stack and exposed. The glass slides are secured in a 3D-printed template to maintain a proper offset between the glass slides while the PDMS cures (step B in figure 9). The assembly of the glass stack and the template is then cured in an oven at 60 °C for 2 h, after which the glass stack is removed from the template, and excess PDMS is cleaned off. Next, a 3D-printed jig is bonded to a 50.8 mm × 76.2 mm glass plate using PDMS (step C in figure 9, photo of the actual jig shown in figure 10(B)), which serves as a stand for the glass stack as well as a mold for casting a rectangular object with a blazed grating on top. The glass stack is placed on the jig at a 30° angle such that the side of the stack with steps completes the top ceiling of a rectangular containment created by the jig and the glass plate, forming a closed cavity (see figure 9(E)).

The rectangular blazed grating object is then cast from this cavity (steps (D) and (E) in figure 9) using an epoxy resin
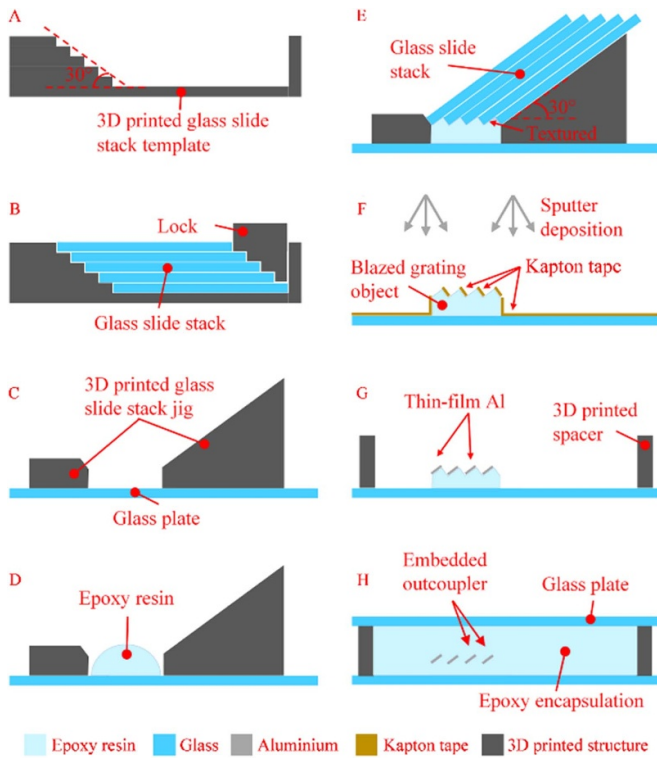
Figure 9. Fabrication steps for making the light guide prototype, after texturizing an array of tilted surfaces and encapsulation.

(MAX CLR). The resin is cured at room temperature for 48 h (step (E) in figure 9). Once the resin is cured, the 3D-printed jig and the glass stack are carefully removed, leaving only the rectangular object on the glass plate. The average thickness of the rectangular object is about 1.5 mm. Note that a silicone mold release agent (Mann Release Technologies Easy Release 200) is sprayed on the area of the glass stack that would be in contact with the resin, prior to dispensing resin and closing off the cavity with the glass stack. This greatly helps with detaching the glass stack from the cured rectangular object. Once the 3D-printed jig and the glass stack are removed, the rectangular blazed grating object is cleaned with isopropyl alcohol (IPA) to get rid of any remaining release agent on the surface. Next, we prepare the glass plate with the rectangular object for sputter coating by masking it with Kapton tape, exposing only the sides of the blazed grating that will become the semi-reflective outcouplers (step (F) in figure 9). We check that these surfaces that will be sputter coated are tilted at the desired 30° angle by inspecting the rectangular object under a microscope (figure 10(F)). The masked glass plate with the rectangular object is then put into an Angstrom Engineering Aeres PVD sputter coater, and an 8 nm thick aluminum film is deposited to achieve a ~50% reflectivity (platform rotation disabled). After sputter coating, the Kapton tape is removed. Next, the sputter coated glass plate is prepared for encapsulation, where a 3D-printed rectangular spacer with a height of 4 mm is bonded to the glass plate using PDMS (step (G) in figure 9). This provides a containment for the epoxy resin (MAX CLR) used for encapsulation. Once the rectangular spacer is adhered to
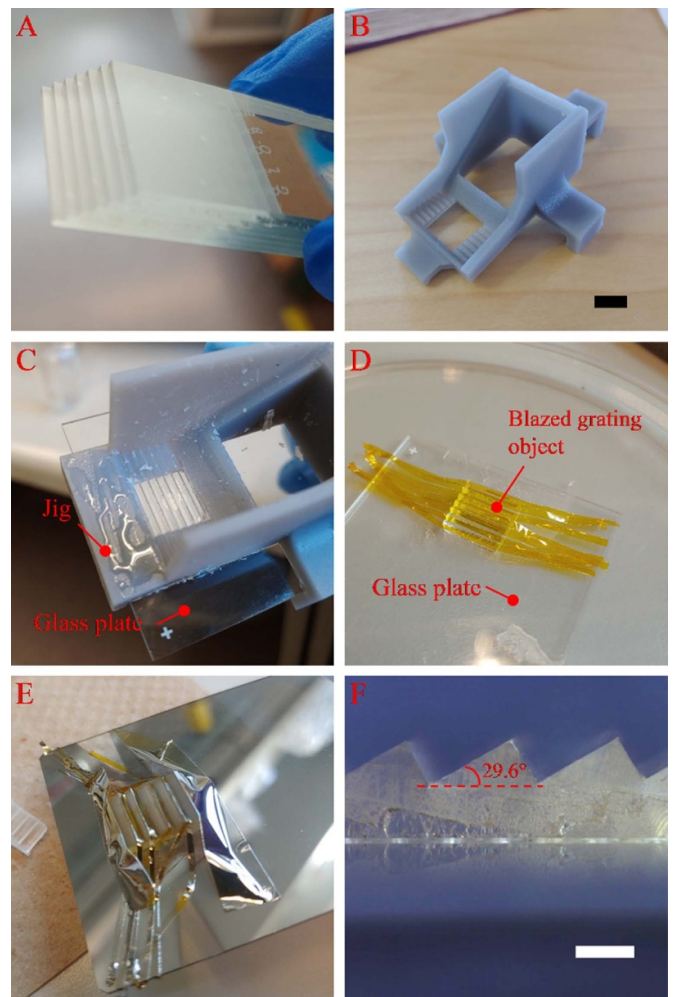

Figure 10. Various photos taken during the making of the blazed grating object at different fabrication steps. (A) Picture of the glass slide array glued with PDMS. The glass slides are offset from each other by 2.08 mm. (B) Picture of the 3D-printed jig/mold for casting the blazed grating object. The black scale bar is 10 mm in length. (C) After the blazed grating object has been cast, and the glass stack removed from the jig. (D) The blazed grating object on the glass plate, masked with Kapton tape. (E) After the blazed grating stack is sputter coated with a thin layer of aluminum. Note that this picture is taken during a sputter coating experiment, so the glass plate is not masked with Kapton tape. (F) The side profile of the blazed grating object is seen under a microscope. The white scale bar is 1 mm in length.

the glass plate, we pour in the resin to the top of the spacer and place another glass plate of the same size to cap it off. The resin is cured at room temperature for 48 h. Figure 10 shows photos of some of the components taken during the fabrication process, and figure 11 shows the final prototype.

2.3. Building an experimental setup using a prism incoupler and an LED light source

The fabricated light guide prototype is evaluated with a test setup built on an optical breadboard. The setup shown in figure 12 is similar to the schematic shown in figure 1, except

Figure 11. The fabricated prototype. Note that there is a visible entrapment of bubbles within the waveguide which did not degas during the encapsulation process. These bubbles do not affect the workings of the prototype.
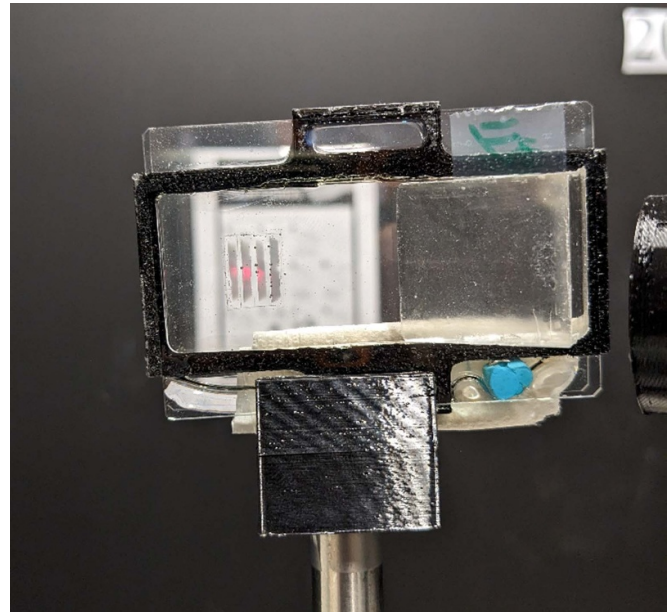

Figure 12. The test setup. The inset shows a close-up view of a PDMS incoupler.

Figure 13. Close-up view of the light guide in the test setup with the camera focused at the diffusive outcouplers, and the light source turned on. Some of the red light diffused out of the light guide by the outcouplers is visible in the outcoupler area.
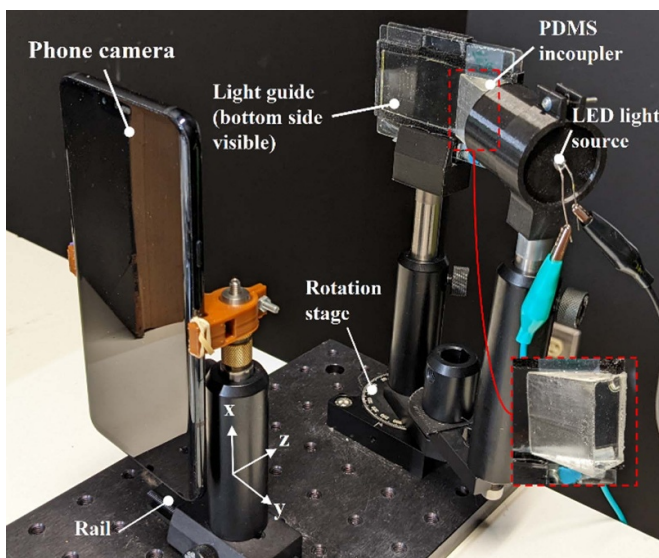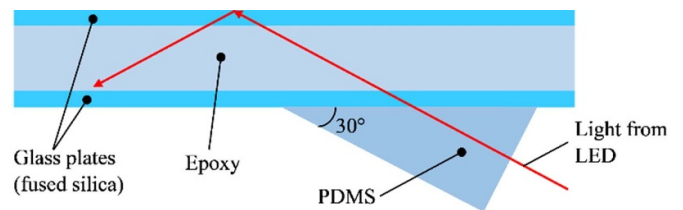

Figure 14. A schematic showing the angular relationship between the light guide, the prism incoupler, and the light coupled into the light guide. The refraction at the boundaries between the different materials is ignored, as their refractive indices are similar.

the eye is replaced with a camera. The setup allows capturing images of the background scenery seen through the outcoupler region of the light guide, as well as the light travelling within the light guide being scattered by the outcouplers. Figure 13 shows a closer-up view of the light guide.

Images are captured with an LG V40 ThinQ smartphone with a 12 MP, f/1.5 image sensor. This smartphone is chosen as it has a manual mode to control and fix camera settings such as the white balance and the exposure time. A red domed through-hole LED diode about 1 mm in diameter is used as a point light source, which is collimated by an aspherical lens with a focal length of 20.1 mm (ACL2520U-A from Thorlabs). The lens is fixed in place relative to the LED, but the lens and the LED can rotate relative to the light guide, so that we can change the angle of incidence of the collimated light with respect to the light guide.

The collimated light is fed into the light guide through a prism-type incoupler that is cast using PDMS. PDMS adheres well with an air-tight seal to the outer cladding of the light guide that is made from fused silica. In addition, the refractive index of the cladding is similar to that of PDMS ($\sim$1.42). The cross section of the prism incoupler forms a right-angle triangle with a base angle of 30° as shown in figure 14, so that light rays entering orthogonally through the incoupler have an incident angle of 60° within the light guide. Note that for simplicity we are ignoring the small differences in the refractive indices between the epoxy encapsulation material, the fused silica glass plate, and the PDMS prism incoupler, which causes the light to slightly refract at the boundaries and results in a couple degrees of deviation for the range of incident angles used. However, the difference in the index of refraction between air and PDMS is taken into account when light enters the incoupler at other angles than perpendicular.

The assembly of the light guide and the light source is placed on a rotation stage, such that they together can be rotated 180 degrees about the *x*-axis. This allows us to observe the scattered light being decoupled through the bottom side of the light guide (same side the prism incoupler is on), as
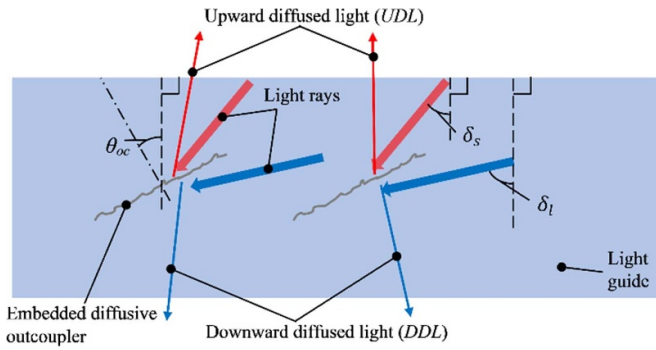
Figure 15. A schematic showing light rays approaching the tilted diffusive outcouplers from both sides. δ_s and δ_l denote special cases δ where $\delta > 90-\theta$ and $\delta < 90-\theta$, respectively.

well as the top side without disturbing the geometrical relationship between the light source and the light guide, i.e. with the collimated light travelling within the light guide at a fixed incident angle. Note that the phone camera we use to encode the captured pictures in the sRGB colorspace, which is gamma-corrected. This produces a discrepancy in the amount of scattered light calculated from the pixel values-based relative luminance. Therefore the effects of the gamma correction need to be cancelled in order to compute the more accurate relative luminance. As such, we first convert the colorspace of the pictures into the linearized CIE-XYZ colorspace using a method discussed in [20], then compute the relative luminance from the pixel values in the linearized pictures.

3. Biasing of the light output

3.1. Theoretical analysis of the light output bias as a function of light incident angle and outcoupler slope

The light travelling within the light guide can approach the outcouplers with both positive and negative attack angles, i.e. either from above or below the plane of each outcoupler. Therefore, the light scattered by the outcouplers can exit the light guide through either the upper surface (upward diffused light (*UDL*)) or the lower surface (downward diffused light (*DDL*)) of the light guide. The ratio between the amount of *UDL* and *DDL* can be biased by adjusting the difference in the angle between the outcoupler tilt θ and the incident angle of the light propagating within the light guide δ, as shown in figure 15.

The light travelling within the light guide can approach the outcouplers with both positive and negative attack angles, i.e. either from above or below the plane of each outcoupler. Therefore, the light scattered by the outcouplers can exit the light guide through either the upper surface (*UDL*) or the lower surface (*DDL*) of the light guide. The ratio between the amount of *UDL* and *DDL* can be biased by adjusting the difference in the angle between the outcoupler tilt θ and the incident angle of the light propagating within the light guide δ, as shown in figure 15.

The analytical expressions for the light exiting the upper or lower surface of the light guide

$$UDL \propto \begin{cases} 0, & \text{if } \delta \geqslant 90° - \theta \\ \cos(\delta + \theta), & \text{else} \end{cases}, \quad (1)$$

$$DDL \propto \begin{cases} 2\sin(\delta)\sin(\theta), & \text{if } \delta \geqslant 90° - \theta \\ \cos(\delta - \theta), & \text{else} \end{cases}, \quad (2)$$

and

$$\delta_c \leqslant \delta \leqslant 90°, \quad (3)$$

where δ_c is the critical angle for TIR. In equation (1), $UDL = 0$ if $\delta \geqslant 90 - \theta$ because the light rays will interact only with the bottom side of the diffuser, sending the reflect-diffused light down toward the *DDL* domain only. Note that when $\delta \geqslant 90 - \theta$ the collimated light propagating within the light guide can approach the bottom side of the diffuser in both downward direction and upward direction, after bouncing off the lower surface of the light guide. Therefore, the light interaction with the diffuser in both scenarios need to be considered for *DDL*. Also, the reflectivity is the same regardless of the side of the diffuser the light is reflect-diffused from. Therefore, θ and δ are the only parameters in the expressions representing the amount of *DDL* and *UDL*. Equations (1) and (2) have been derived based on a number of assumptions: (1) there is no loss of energy in any stage of light propagation, (2) the rays propagating within the light guide are perfectly collimated, (3) the light rays transmitted through the outcoupler experience no diffusion, (4) all of the light reflecting from the outcouplers is diffused within the same reflection domain, e.g. light reflecting from the outcoupler in the *UDL* domain is diffused and remains strictly in the *UDL* realm, (5) the external surfaces of the light guide are 100% transmissive, and (6) for simplicity, the light only interacts once with one single outcoupler. For a fixed $\theta = 30°$, the ratio *UDL/DDL* as a function of δ can be plotted as shown by the solid red line labelled 'Analytical *UDL/DDL*, tilted diffuser' in figure 22. Note that for $\delta \geqslant 60°$, under ideal conditions mentioned above, one can theoretically achieve a 100% downward bias (*UDL/DDL* = 0), because the light rays will only reflect and scatter from the bottom side of the outcouplers.

3.2. Simulation of the light output bias

The simple analytical model does not consider any secondary effects such as the light transmitted through or scattered by the diffusive outcoupler that continues to propagate within the light guide by TIR, and then interact with another outcoupler for the second time or more. These secondary effects are hard to model analytically on a single ray basis, as the propagation is stochastic in nature, especially in the absence of knowledge about the scatter profile of the outcouplers. Thus, we create a model of the light guide with tilted outcouplers in ray tracing software Zemax OpticStudio and simulate light propagating in the light guide to observe the consequences of the secondary effects and how the light behavior deviates from the
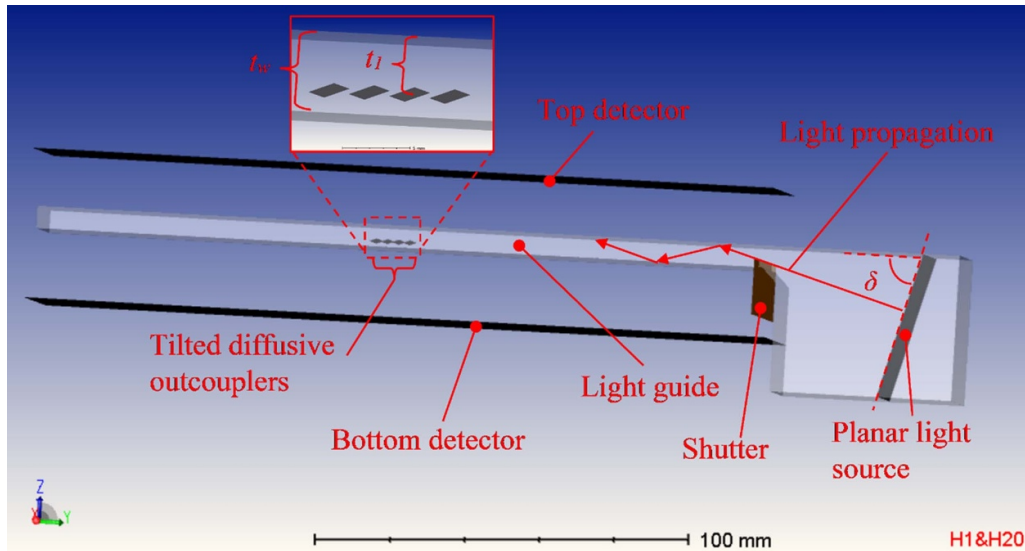
Figure 16. The simulation setup in OpticStudio.

Table 1. OpticStudio simulation parameters and their values.

Parameter	Value
Depth of outcouplers t_1	1.5 mm
Detector size, both top and bottom, $x \times y$	50 mm $\times$ 200 mm
Dimensions of the waveguide, x (width) $\times y$ (length) $\times z$ (height, tw)	30 mm $\times$ 200 mm $\times$ 6 mm
Number of outcouplers	4
Outcoupler dimensions, $x \times y$	30 mm $\times$ 2 mm
Outcoupler array periodicity in y	3 mm
Outcoupler tilt angle relative to z-axis	30°
Outcoupler reflectivity	50%
Range of incident angle δ	45°–75°
Dimensions of the planar light source, $x \times y$	30 mm $\times$ 40 mm
Gap between light guide and detector in z-axis	16 mm for both top and bottom detectors
Light guide refractive index	1.5
# of analysis rays	1 $\times$ 106
Light source power	1 Watt

into the light guide. The incident angle of the rays is then varied by controlling the tilt angle of the planar light source. The tilt angle of the outcoupler between the outcoupler surface normal and the vertical z-axis is fixed at 30°. We assume the scattering of the outcouplers to be Lambertian, using the ABg scattering model with $g = 0$.

The reason we use the ABg model-based Lambertian profile instead of the built-in Lambertian scatter model is because the scattering in the reflection and the transmission domains can be defined independently. Note that we assume the outcouplers scatter only in the reflection domain, and there is no transmissive scattering. We then run a set of simulations with different planar light source tilt angles δ ranging from 45° to 75°. The light scattered by the outcouplers that is decoupled from the light guide is captured by either the bottom or the top detector. The amount of light captured by each detector is evaluated in terms of the irradiance. The intensity profile of the scattered light intercepted by each of the bottom and the top detectors is shown in figure 17.

4. Experimental results

4.1. Demonstrating the see-through transparency of the light guide prototypes

To show that both light guide prototypes with either the lithography-based planar diffuser outcoupler or the replication-based tilted outcoupler array described in section 2.2 are visually clear, we take pictures of the prototypes against background objects, as shown in in figures 18 and 19. As intended, the background object, a page on a book and a public announcement bulletin on washing hands, is visible through the outcoupler region without any distortion or occlusion, unlike methods that use micro-features to

simple analytical model. Figure 16 shows the simulation setup in OpticStudio, and the parameters and their values used in the simulation are given in table 1.

In the simulation, the planar light source orthogonally emits perfectly collimated light, so all of the rays travelling within the light guide, prior to being scattered by the outcouplers, are parallel to each other. Note that the planar light source is within an extended and enlarged section of the waveguide. This is to avoid refraction as light rays enter the light guide and make the tilt angle of the planar light source with respect to the horizontal y-axis equal to the incident angle of the rays coupled
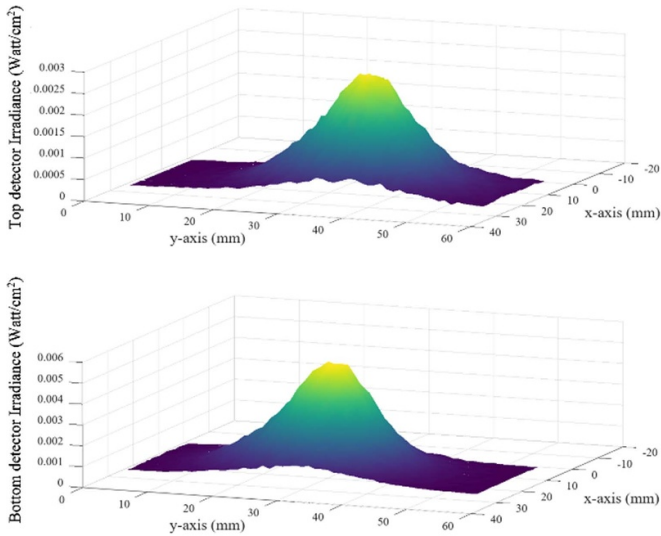
Figure 17. The intensity profile of the light scattered from the light guide, intercepted by each of the detectors. The tilt angle of the diffuser $\theta = 30°$, and the light incident angle $\delta = 50°$.

Figure 19. Background object seen through the tilted outcoupler light guide prototype, ∼1.5 m away from the light guide. Left-side image: camera focused at the light guide, ∼15 cm away, such that the semi-transparent outcouplers are visible. Right-side image: camera focused at the bulletin in the background, ∼1.5 m away. The inset at the bottom left corner is a close-up view of the square area highlighted by the red dashed line, showing the bulletin is visible and undistorted through the outcouplers, and the outcouplers only reduce the local brightness in some areas of the bulletin. The incident angle of the laser beam within the light guide is ∼30°.
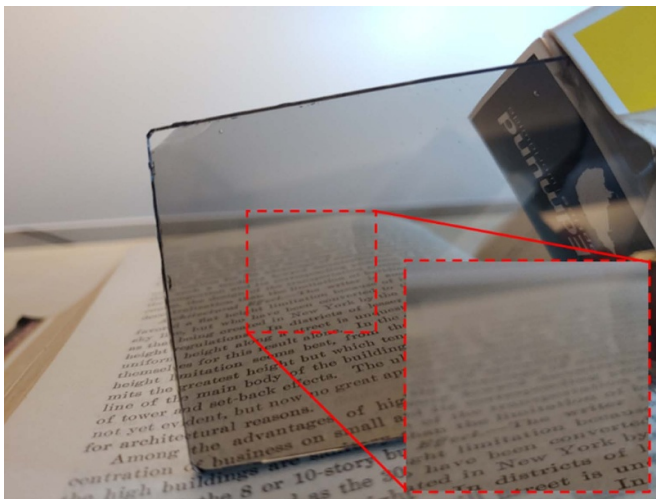

Figure 18. Demonstration of the see-through transparency of the light diffuser made using the photolithographic texturization method discussed in section 2.1.

extract light such as [15, 18]; the presence of the outcoupler only darkens the imaged bulletin locally.

4.2. Demonstration of the light output biasing with different light incident angles

We measure the amount of light scattered by the outcouplers emanating from the upper and the lower surfaces of the light guide with the tilted outcoupler array, using the test setup shown in section 2.3. The amount of the scattered light is measured in terms of the relative luminance calculated from the average pixel values in the pictures of the outcouplers, taken through each side of the light guide. In the test setup,
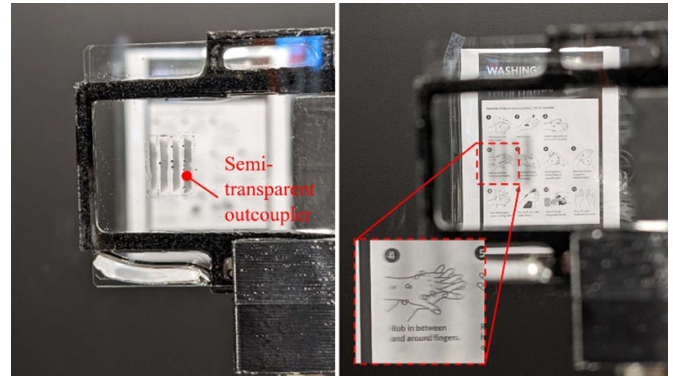
the camera is ∼10 cm away from the light guide, and the camera focal length is adjusted such that the outcouplers are in focus. To assess the effects of changing the incident angle δ on the *UDL/DDL* bias ratio, we rotate the LED light source to change the approach angle of the collimated light relative to the prism incoupler. The LED light source is rotated discretely such that δ is increased in increments of approximately 5° from 50° to 73.2°. Because the collimated beam from the light source needs to refract into the light guide through the prism incoupler, and due to the lack of fine adjustments for the rotation of the LED light source, the angular gap between our measurement points is not constant at five degrees. At each incident angle δ, we take a picture of the outcoupler region through the bottom side of the light guide to measure the amount of DDL and take another picture through the upper surface of the light guide for the UDL measurement after rotating the light guide assembly by 180 degrees. Figure 20. Shows the pictures of the light guide taken through both sides at each δ. The amount of *UDL* at each δ is estimated from the pictures taken through the bottom side of the waveguide, whereas the amount of *DDL* is estimated from the top side pictures, as shown in figure 20. The ratio between the empirical *UDL* and *DDL* values at each δ corresponds to the relative luminance of the outcouplers, which is plotted against the theoretical and simulated bias ratios in figure 21. As can be seen, the empirical *UDL/DDL* ratio curve mostly matches the simulated ratio for the tilted diffusers. We believe the slight mismatch could be attributed to imperfections in the fabricated light guide such as embedded air bubbles in the outcoupler region, as well, the collimation of light from the light source is not perfect with a ∼5° divergence, due to the LED diode being larger than an
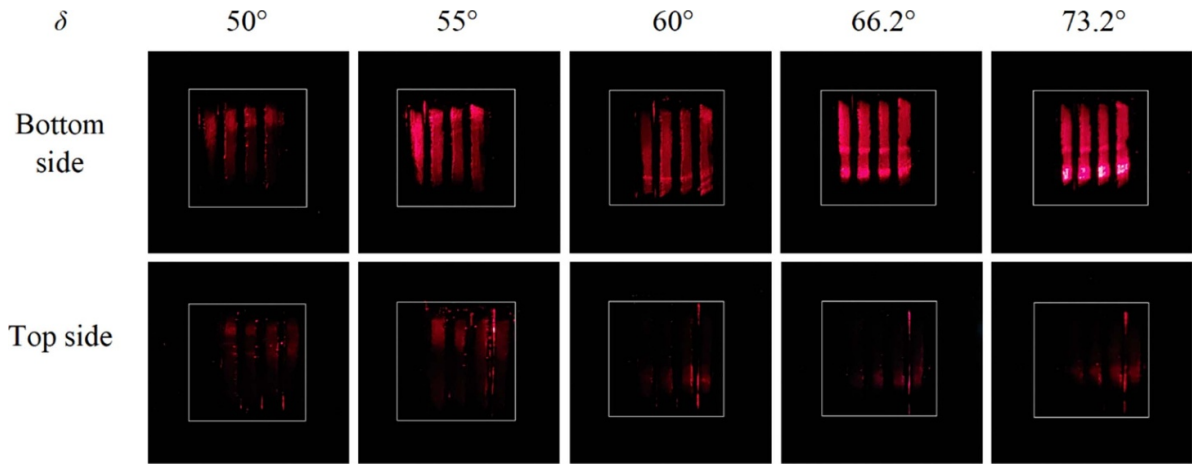
Figure 20. Pictures of the outcoupler illuminated by the light travelling within the light guide, taken through the upper and the lower surfaces of the light guide at each light incident angle δ. The white squares outline the area from which we calculate the average relative luminance. The tilt angle of the outcoupler $\theta = 30°$.
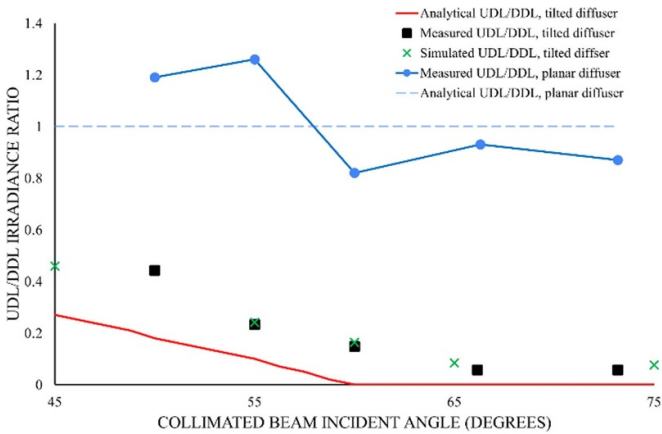

Figure 21. The empirical *UDL/DDL* ratio at different light incident angle estimated from the relative luminance of the pictures shown in figure 20, compared to the theoretical and simulated ratios. Note that the relative luminance values used to calculate the empirical *UDL/DDL* ratio have been adjusted to undo the effects of gamma correction. The graph also includes the analytical and measured *UDL/DDL* for the light guide with a planar (horizontal) diffuser buried half-way in the light guide.

ideal point source. However, we do notice that both the empirical and the simulated ratio curves deviate greatly from the theoretical model, although they all exhibit similar trends. This is because the theoretical model does not consider the secondary effects mentioned earlier.

4.3. Demonstration of other applications of the light guide with the photolithography-based planar diffuser

We believe the light guide with a photolithographically textured planar diffuser has a couple of other potential use-cases, for example as a visually-clear projection screen and a planar diffusive light source, as shown in figure 22.
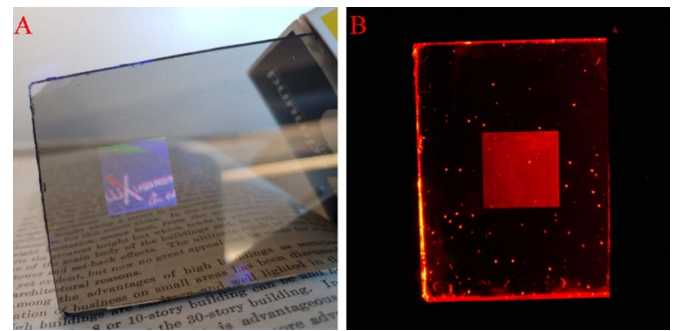

Figure 22. Demonstration of light diffusing from the planar diffuser prototype. (A) The prototype is used as a projection screen, with an image projected onto the semi-reflective diffuse area. Because the diffusive surface scatters light, the projected image is seen at a non-specular viewpoint. (B) The prototype is used as a diffusive light source. Light is coupled into the light guide through the edge of the light guide. The light travelling within the light guide is scattered by the diffusive surface, making the diffusive area visible.

5. Conclusions

We present a simple method of creating a rough surface on SU-8 films using PET photomasks. We show that the roughness and the diffusivity of the SU-8 films can be changed by varying the number of photomask layers and the exposure time. Alternatively, we show that texturization on tilted surfaces can be achieved by using a stack of frosted glass slides as a mold. We build a planar light guide prototype with an embedded surface textured using our texturization technique and coated in a thin metal layer, to show that the textured surface diffuses light and is visually clear. We also show analytically and with simulation results that we can bias the amount of light being diffused from either side of the light guide, by changing the relative angle between the tilt angle of the embedded diffusive outcouplers and the incident angle of the light approaching the outcouplers. To verify our analytical model of the light output

bias, we build another light guide prototype with tilted textured surfaces using 3D printing, metallization through sputter coating, and resin casting processes. The measurements of the light output bias taken from this prototype with different relative angles between the diffusive outcouplers and the light rays are in good agreement with the simulation results and exhibit a similar trend to the analytical model.

Data availability statement

All data that support the findings of this study are included within the article (and any supplementary files).

Acknowledgments

ORCID iD

Hongbae Park ⬤ https://orcid.org/0000-0002-3092-412X

References

[1] Xu M and Hua H 2019 Methods of optimizing and evaluating geometrical lightguides with microstructure mirrors for augmented reality displays *Opt. Express* **23** 5523–43

[2] Lee Y, Yoon G and Yoon J 2019 Mass-producible structural design and fabrication method for a slim lightguide plate having inverse-trapezoidal light out-couplers *J. Micromech. Microeng.* **29** 035001

[3] Amitai Y 2011 Light guide optical device *US Patent* US8004765B2

[4] Yan Z, Du C and Zhang L 2020 Surface micro-reflector array for augmented reality display *IEEE Photon. J.* **12** 1–9

[5] Zhang Y and Fang F 2019 Development of planar diffractive waveguides in optical see-through head-mounted displays *Precis. Eng.* **60** 482–96

[6] Mukawa H, Akutsu K, Matsumura I, Nakano S, Yoshida T, Kuwahara M, Aiki K and Ogawa M 2008 A full color eyewear display using holographic planar waveguides *Digest Tech. Papers SID Int. Symp.'08* (*Los Angeles*, *18–23 May 2008*) pp 89–92

[7] Nichol A and Coleman Z 2014 Method of manufacturing a light input coupler and lightguide *US Patent* US8917962B1

[8] Soomro S and Urey H 2016 Design, fabrication and characterization of transparent retro-reflective screen *Opt. Express* **24** 24232–41

[9] Hsu C, Zhen B, Qiu W, Shapira O, DeLacy B, Joannopoulos J and Soljačić M 2014 Transparent displays enabled by resonant nanoparticle scattering *Nat. Commun.* **5** 3152

[10] Nicholson-Smith C, Knopf G and Bordatchev E 2016 Controlled guidance of light through a flexible optical waveguide sheet *Proc. SPIE* **9759** 97590C

[11] Vasiliev M, Alameh K, Badshah M, Kim S and Nur-E-Alam M 2018 Semi-transparent energy-harvesting solar concentrator windows employing infrared transmission-enhanced glass and large-area microstructured diffractive elements *Photonics* **5** 25

[12] Röhm GmbH ACRYLITE® LED light guiding edge lit (Roehm America LLC) (available at: www.acrylite.co/3735b-endlighten-led-technical-brochure.html) (Accessed 20 June 2022)

[13] Klammt S, Neyer A and Müller H 2012 Microoptics for efficient redirection of sunlight *Opt. Express* **51** 2051–6

[14] Jakubowsky M, Hubschneider C, Neyer A, Fang Y and De Boer J 2019 Microstructured light guiding plate for single-sided light emission as light source for room illumination *Appl. Opt.* **58** 76

[15] Green R, Knopf G and Bordatchev E 2017 Multi-layered fabrication of large area PDMS flexible optical light guide sheets *Proc. SPIE* **10101** 101010Y

[16] Pan J and Hu Y 2012 Light-guide plate using periodical and single-sized microstructures to create a uniform backlight system *Opt. Lett.* **37** 3726

[17] Yeon J, Lee J, Lee H, Song H, Mun Y, Choi Y, Choi H, Lee S and Yoon J-B 2012 An effective light-extracting microstructure for a single-sheet backlight unit for liquid crystal display *J. Micromech. Microeng.* **22** 095006

[18] Maimone A, Lanman D, Rathinavel K, Luebke D and Fuchs H 2014 Pinlight displays: wide field of view augmented reality eyeglasses using defocused point light sources *ACM Trans. Graph.* **33** 1–11

[19] Park H, Hoskinson R and Stoeber B 2019 Embedded Concave Micromirror Array-based See-through Light Field Near-eye Display *ACM SIGGRAPH Asia (Brisbane, Australia, November 2019)* (https://doi.org/10.1145/3355088.3365141)

[20] Stokes M, Anderson M, Chandrasekar S and Motta R A standard default color space for the internet—sRGB *The World Wide Web Consortium* (available at: www.w3.org/Graphics/Color/sRGB.html) (Accessed 4 July 2022)